Sliding Mode Observer Driver IC Integrated Gate Driver for Sensorless Speed Control of Wide Power Range of PMSMs

Jimin Oh, Minki Kim, Sewan Heo, Jung-Hee Suk, Yil Suk Yang, Ki-Tae Park, and Jinsung Kim

This work proposes a highly efficient sensorless motor driver chip for various permanent-magnet synchronous motors (PMSMs) in a wide power range. The motor driver chip is composed of two important parts. The digital part is a sensorless controller consisting mainly of an angle estimation block and a speed control block. The analog part consists of a gate driver, which is able to sense the phase current of a motor. The sensorless algorithms adapted in this paper include a sliding mode observer (SMO) method that has high robust characteristics regarding parameter variations of PMSMs. Fabricated SMO chips detect back electromotive force signals. Furthermore, motor current–sensing blocks are included with a 10-bit successive approximation analog-to-digital converter and various gain current amplifiers for proper sensorless operations. Through a fabricated SMO chip, we were able to demonstrate rated powers of 32 W, 200 W, and 1,500 W.

Keywords: Wide power range of motors, sensorless speed control, sliding mode observer driver IC, integrated gate driver.

I. Introduction

Permanent-magnet synchronous motors (PMSMs) are widely used in home appliances and industries; in particular, the automotive industry. Various rated powers of PMSMs have been implemented, such as 10 W to 100 W motors used in the drying fans of washing machines [1], 100 W to 1,000 W motors used in refrigerator compressors [2], and 1 kW to 5 kW motors used in the inner/outer compressors of air conditioners, not to mention in washing machine tubes, electric cars, and other applications [3]–[4]. To operate PMSMs of different rated power levels, a related system needs to be able to apply different types of inverters and driver conditions [2], [5].

Several studies have been conducted using digital processor devices, such as a digital signal processor (DSP) [6]–[7] or a field-programmable gate array (FPGA) [8]–[11] to operate various motors. An FPGA has been used to operate full digital components and for high-speed processing but has a weak point in that it cannot be fabricated using analog parts. A DSP has many advantages in that it can conduct sophisticated and elaborate arithmetic calculations but is a bulky device that cannot be optimized in terms of size and cost.

In this work, an analog and digital mixed application-specific integrated circuit for motor controllers (digital) and gate drivers is implemented with a current sensing (analog) capability for obtaining high-speed calculations, thereby reducing system costs.

In particular, control methods are adapted to sensorless controls for high performance and low cost. Sensorless controls can be divided into observer-based motor models [2]–[4], and high-frequency signal injection [8], [10]. To operate motors, a

sliding mode observer (SMO) method is implemented owing to the various rated motor powers with different motor model parameters, such as phase resistance, inductance, and pole [6]–[7]. In what follows, the target motor model and conventional SMO method are described first, and the fabricated chip technologies used for various motors are then discussed.

This paper demonstrates different motor modules, including a fabricated IC chip, and evaluates the abilities of various rated powers of PMSMs, from tens to thousands of watts. Experimental results show the characteristics of speed control and system efficiency of the proposed model, and compare its capabilities with existing commercial modules.

II. Motor Model and SMO Method

1. Motor Model

Given PMSM currents i_α and i_β, the actual dynamics of each can be expressed as a stationary two-phase reference frame in terms of the nominal values of phase resistance R_s and inductance L_s as follows:

$$L_s \frac{di_\alpha}{dt} = v_\alpha - R_s i_\alpha - e_\alpha, \tag{1}$$

$$L_s \frac{di_\beta}{dt} = v_\beta - R_s i_\beta - e_\beta, \tag{2}$$

where e_α and e_β are the electromotive forces (EMFs) induced by the permanent magnet of a PMSM and are given by

$$e_\alpha = -\psi_0 \omega \sin\theta, \qquad e_\beta = \psi_0 \omega \cos\theta, \tag{3}$$

where ψ_0 is the linkage flux induced by the magnets; ω_e and θ are the electrical speed and position of the rotor, respectively; θ is the angle between the first phase axis and the axis of the magnet north pole.

2. SMO Method

The α, β model of a PMSM in a stationary reference frame is characterized by

$$\frac{d\mathbf{i}_s}{dt} = \mathbf{A}\mathbf{i}_s + \mathbf{B}\mathbf{v}_s + K_E \mathbf{v}_i, \tag{4}$$

where $\mathbf{i}_s = [i_\alpha \, i_\beta]^T$ indicates a stationary α, β current vector; $\mathbf{v}_s = [v_\alpha \, v_\beta]^T$ is a stationary α, β voltage vector; $\mathbf{v}_i = [-\omega\sin\theta \; \omega\cos\theta \,]^T$ is a back electromotive force (BEMF) vector; $\mathbf{A} = (-R_s/L_s)\mathbf{I}$, $\mathbf{B} = (1/L_s)\mathbf{I}$; $\mathbf{I}$ is a 2×2 identity matrix; and K_E is an EMF constant. The α, β estimated current model of a PMSM is provided by

$$\frac{d\hat{\mathbf{i}}_s}{dt} = \mathbf{A}\hat{\mathbf{i}}_s + \mathbf{B}\mathbf{v}_s + G_{sw}\mathrm{sgn}(\hat{\mathbf{i}}_s - \mathbf{i}_s), \tag{5}$$

where $\hat{\mathbf{i}}_s = [\hat{i}_\alpha \hat{i}_\beta]^T$ is the estimated value of i_s, G_{sw} is the sensorless observer switching gain, and $\mathrm{sgn}(\hat{\mathbf{i}}_s - \mathbf{i}_s) = [\mathrm{sgn}(\hat{i}_\alpha - i_\alpha) \; \mathrm{sgn}(\hat{i}_\beta - i_\beta)]^T$. Here, G_{sw} is determined through a theoretical value from various speed-control experiments.

A sliding hyperplane, S, is designed using the state variables, and in this case, the stator currents using the switching functions are described as

$$S = \hat{\mathbf{i}}_s - \mathbf{i}_s \equiv \mathbf{e}_s = 0. \tag{6}$$

The dynamic of the estimation error ($\mathbf{e}_s$) is obtained by subtracting (4) from (5) as follows:

$$\frac{d\mathbf{e}_s}{dt} = \mathbf{A}\mathbf{e}_s - K_E \mathbf{v}_i + G_{sw}\mathrm{sgn}(\mathbf{e}_s). \tag{7}$$

To satisfy necessary conditions for sliding mode convergence, G_{sw} must be chosen to satisfy $\mathbf{e}_s\mathbf{e}_s^T < 0$ with a Lyapunov function. Using equivalent control design methods, an expression for the error equation is obtained as follows:

$$\frac{d\mathbf{e}_s}{dt} = \mathbf{e}_s = 0. \tag{8}$$

Hence, the characteristics of the SMO on the sliding hyperplane can be defined as

$$Z \equiv G_{sw}\mathrm{sgn}(\mathbf{e}_s) = K_E \mathbf{v}_i$$
$$Z = \begin{bmatrix} Z_\alpha \\ Z_\beta \end{bmatrix} = K_E \begin{bmatrix} -\omega\sin\theta \\ \omega\cos\theta \end{bmatrix}, \tag{9}$$

where Z is the switching signal regarding the α, β current errors; Z contains the information of the estimated BEMF. The conventional method using the signum function in (9) requires the low-pass filter of switching signal Z to eliminate the high-frequency signals of Z that cause signal delays and disturbances [6]. The proposed method, on the other hand, can be achieved without a low-pass filter using a linear function that the error of the currents compensates linearly. The rotor position, $\hat{\theta}$, can then be obtained from (9) as follows:

$$\hat{\theta} = -\tan^{-1}(e_\alpha / e_\beta). \tag{10}$$

III. Control Schemes of Fabricated PMSM Drivers

The PMSM module shown in Fig. 1 has inverters and a motor driver chip. The inverters are implemented using power MOSFETs (NXP BUK956R1-100E) with a two-level voltage source inverter. The fabricated PMSM driver chip consists of two parts — one is a sensorless PMSM controller block, and the other is a gate driver block with a current sensing section and I2C controller.
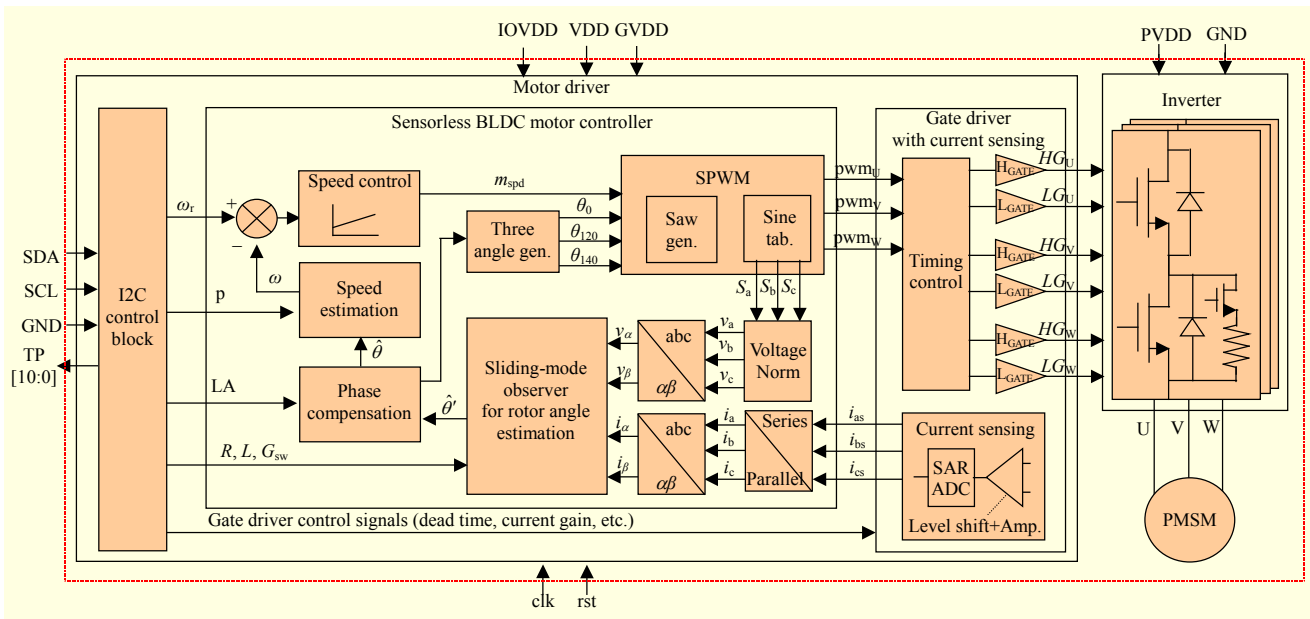
Fig. 1. Architecture of BLDC power module.

1. Sensorless PMSM Controller

The sensorless PMSM controller has several functions, including motor position estimation, phase compensation, motor speed estimation, speed control, and pulse-width modulation (PWM) signal generation.

A. Motor Positon Estimation

Three phase voltage signals are input to the motor; these are PWM type signals. For sensing voltage signals from PWM signals, low-pass filters are required. Because of the extra components and signal delays, the sine signals in the sinusoidal pulse-width modulation (SPWM) block and input voltage in the inverters are implemented in the "Voltage Norm" block shown in Fig. 1 [9]–[10]. This method is useful in terms of integrated sensorless chips that generate no delay or signal distortions. Three phase current signals to the motor are detected from the gate driver sensing blocks. The signals from the sensing blocks form serialized outputs, i_{as}, i_{bs}, i_{cs}, each of which is converted into parallel signals, i_a, i_b, and i_c, respectively, in series–parallel blocks. The three phase voltage and three current signals are axis-converted from three phase coordinate signals to two stationary coordinate signals, α and β.
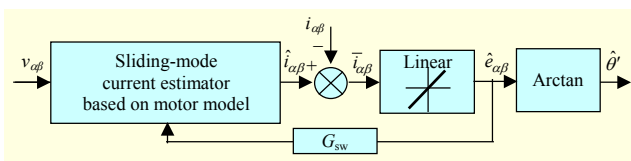

Fig. 2. SMO for angle estimation.

These signals are put into an SMO block to generate an uncompensated motor position, $\hat{\theta}'$.

The two stationary coordinate signals, α and β, of the voltages and currents are proposed in the SMO for the angle calculation block, as shown in Fig. 2. The voltages are calculated to estimate the currents through the previous motor models. The real currents from the sensing currents are compared to the estimated currents from the sliding-mode current estimator. The generated current differences, $\bar{i}_\alpha$ and $\bar{i}_\beta$, are used for generating the estimated BEMF signals, $\hat{e}_\alpha$ and $\hat{e}_\beta$, respectively, in a linear function. The linear function compensates the signal errors linearly in that a signum function compensates the errors using a constant step size. The slope value is 0.5. The outputs of the signum function have high-frequency signal components; thus, a low-pass filter and passive components are needed. Both the sigmoid and linear functions are methods in which errors are compensated in an error-proportional step [3]–[4], [7]. In terms of fabricating the chip, a linear function method is easy to implement compared with a sigmoid function. The estimated BEMF signals $\hat{e}_\alpha$ and $\hat{e}_\beta$ are put into an Arctan block to calculate the uncompensated motor position $\hat{\theta}'$ [12]. The initial position in an Arctan block is set to the point at which the estimated BEMF alpha signal $\hat{e}_\alpha$ changes from negative to positive. The angle sensitivity is 0.5 degrees with a 10-bit register, and the input signals of the phase currents and voltages are controlled at 20 kHz (50 µs).

B. Phase Compensation

The estimated motor position from the angle calculation

block is affected by the motor parameters, sensorless gain, and model uncertainties. In this case, using an external I2C control signal, the estimated angle is revised into a compensated motor position $\hat{\theta}$ with a phase compensation. This compensation is strongly related with the phase current control, as determined experimentally [6].

C. Speed Estimation and Control

In the speed estimation block, the estimated angle and phase compensation are implemented using a motor pole from the I2C control block. The sensitivity of the speed estimation is designed using 1 rpm and an update frequency to calculate a speed of 1 kHz (1 ms). Furthermore, the calculated speed may have an offset speed; thus, the offset speed is controlled from 0 rpm to 7 rpm by the I2C control block.

The estimated speed is compared with a reference speed from the I2C control block, and is controlled to minimize the error between the reference and estimated speeds. The speed control time is also 1 ms. If a reference speed is higher than the estimated speed, then the value of control signal m_{spd} (see Fig. 1) is increased from the previous m_{spd}, and if the reference speed is lower than the estimated speed, then m_{spd} is decreased from the previous m_{spd}. This method appears to be a simple but powerful and effective way of fabricating an IC chip.

D. PWM Signal Generation

In the PWM signal block, the compensated position signal and control signal are implemented to generate three phase PWM signals [11]. The frequency of the PWM is 20 kHz and the reference signal frequency of the sawtooth wave is the same. First, the compensated motor position $\hat{\theta}$ can be used to generate three phase position signals, $\hat{\theta}_0$, $\hat{\theta}_{120}$, and $\hat{\theta}_{240}$, such that two of the three phase position signals have a 120-degree phase difference. These signals are converted into three phase sine signals, S_a, S_b, and S_c, by sine look-up tables, one of which is a 14-bit signed sinusoidal table and the other is a 14-bit signed space vector sinusoidal table. These two tables are selected by the I2C control block. The three phase sine signals and control signal are operated to choose three phase PWM signals pwm_a, pwm_b, and pwm_c.

2. Gate Diver with Current Sensing Circuits

A gate driver block includes two main blocks, one of which is a high-side gate driver, and the other is a low-side gate driver. An external power MOSFET utilizes an *N*-channel MOSFET; thus, the high-side driver is implemented using a bootstrap capacitor and diode, as shown in Fig. 3. In Fig. 3, HGATE is
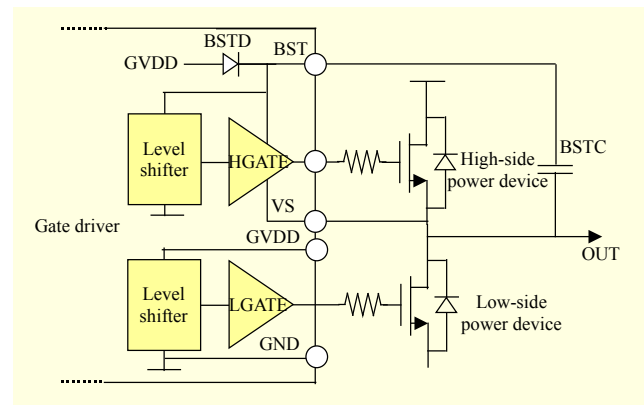

Fig. 3. High-side gate drivers.

used to select one output between V_{BST} and V_s. The voltage at the point "BST" in Fig. 3 is made higher than OUT by using an external bootstrap cap (BSTC). The voltage of GVDD is 5 V, and the bootstrap diode (BSTD) works as a current supplier to increase the voltage of the BST. If a high-side level shifter is on, then the output of HGATE is the voltage of BST used to turn on the high-side power MOSFET. If the high side is off, then the output is the voltage of the source such that the high-side power MOSFET is off. A low-side power MOSFET uses LGATE to select the output between the voltage of the GVDD and GND; LGATE is operated using a low-side level shifter.

An additional gate driver function includes control of the dead time between the high- and low-side PWMs. The dead time is controlled by the I2C control block from 30 ns to 380 ns. Over-temperature protection and an under-voltage lock-out function are also included. Three phase voltages and currents to the motor operation are needed to adapt the previous SMO algorithms. As previously described, three phase voltages are induced by three sine signals with an input voltage to the power MOSFET.

On the other hand, three phase currents are detected directly such that the currents are influenced by inner motor resistance and inductance. There are many methods for detecting currents — the use of current sensors [13]–[14], shunt resistors [2], and current mirrors [15]. This paper suggests using a MOSFET for sensing and a shunt resistor, as shown in Fig. 4(a). The MOSFET and shunt resistor are set in parallel with a low-side power MOSFET. This current sensing method can be a bipolar current sensing circuit. With a level-shifting circuit and an internal amplifier, a phase current is detected using a digital gain control. The on-resistance of a MOSFET is approximately 5 mΩ and the shunt resistor is 1 kΩ; the sensing voltage can be determined by the on-resistance of the MOSFET. The output of the internal amplifier is varied by the gain of the amplifier with a range of 1 to 16, as shown in Fig. 4(b). A controlled output based on the gain value is connected to a 10-bit analogue-to-
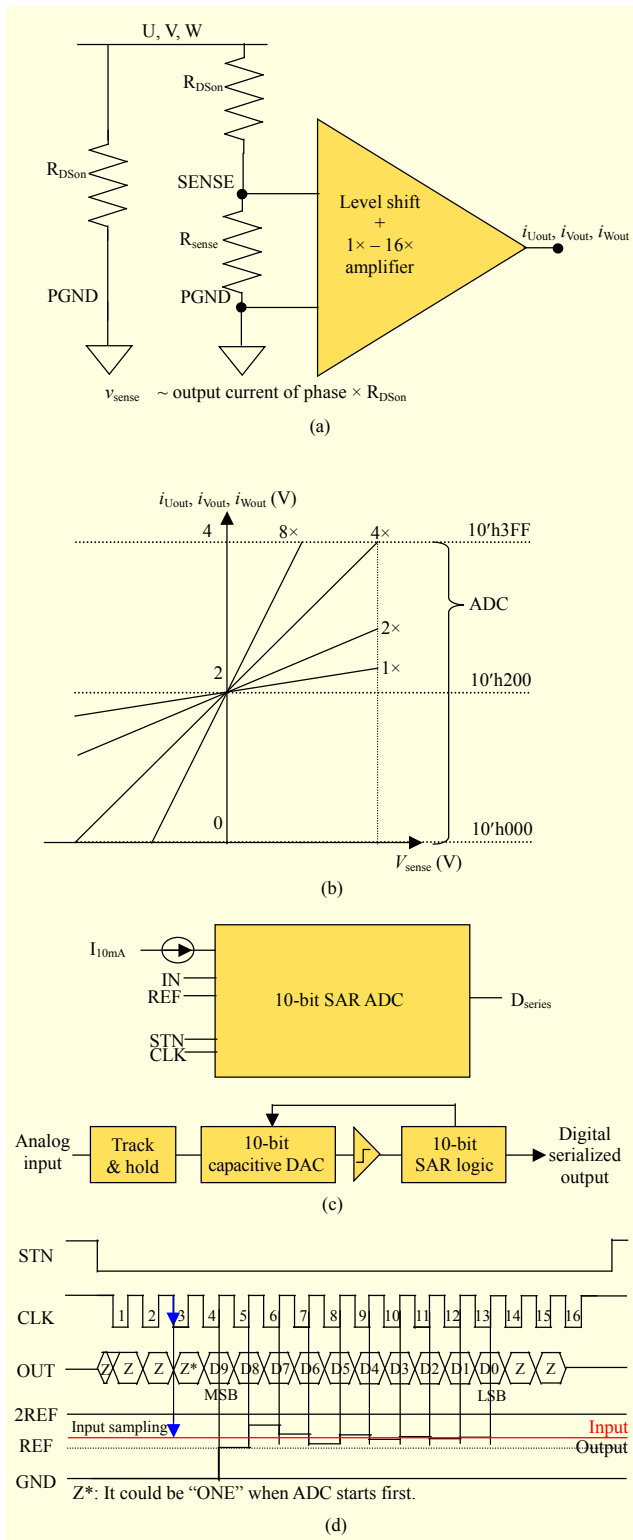
Fig. 4. (a) Current sensing circuits, (b) variable gain control, (c) 10-bit SAR ADC, and (d) ADC control description.

digital converter (ADC) to convert the digital signals.

In Fig. 4(c), the input signals include a reference, a 10 mA current source, an STN, and a CLK. The fabricated 10-bit
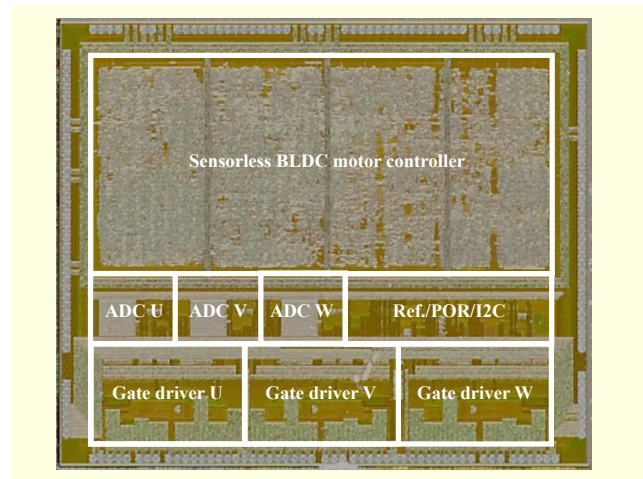

Fig. 5. Photograph of motor driver chip.

ADC functions to track and hold an analog signal, and successive approximation (SAR) logic signals are fed back to a capacitive DAC. Figure 4(d) shows the ADC control description. After a 13-bit clock signal, a digital output is achieved. ADC operating signals such as STN and CLK are provided from the fabricated chip. CLK is synchronized with PWM signals, and its frequency is 1.6 MHz.

Figure 5 shows a photograph of the motor driver chip. The driver chip is manufactured using a 0.18 μm BCD process. The operating frequency is 20 MHz and the chip size is 4.4 mm × 3 mm. The I/O (IOVDD) and core voltage (VDD) are 5 V and 1.8 V, respectively, and the gate driver voltage (GVDD) is 5 V. A 64-pin QFN-type chip package is used.

IV. Experimental Results

1. Experimental Environment

Figure 6 shows the experimental setup using a 1,500 W PMSM. The PMSM is connected with a hysteresis electric load through a fabricated mechanical coupling. Each motor is connected through a proper electric load. The PMSM power module is composed of a motor driver and inverters. The module is connected with an I2C controller PC, total phase AARDVARK I2C/SPI to control the motor speed, phase compensation, sensorless parameters, gain, and so on. The monitoring PC for the test pins is also connected to 11-bit TP pins. The DAC device is an analog ADC Analyzer™ Version 4.8.0. A high-voltage Armel 125 V/160 A DC supplier and Agilent N6705B DC supplier are implemented to operate the PMSM power module. The motor analyzer used for torque detection is a Sugawara PC-EMA, and the power analyzer is a Yokogawa WT1600. The gate signals and phase currents are detected using a LeCroy WR610Zi oscilloscope. The operating
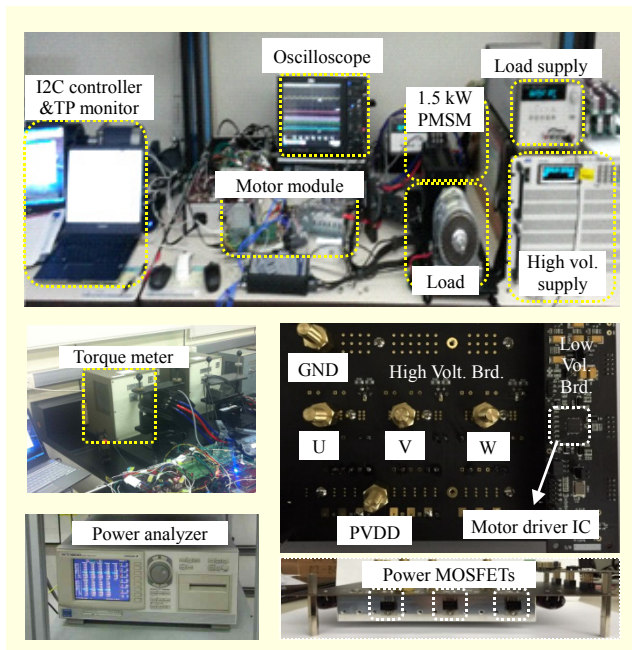
Fig. 6. Experimental environment.

Table 1. Target PMSM specifications.

Motor names	BL55B	D0231	D1536
Manufacturers	Moatech (Korea)	TMtechi (Korea)	
Rated output power (W)	32	200	1,500
Rated voltage (V)	24	24	48
Rated current (A)	2.3	11.7	33.2
Number of poles	10	4	4
Rated speed (rpm)	2,500	3,000	3,000
Rated torque (N·m)	0.12	0.66	4.78
Axis inductance (mH)	1.45	0.62[1]	0.20
Phase resistance (Ω)	0.90	0.29[1]	0.04
Torque constant (N·m/A)	0.06	0.08	0.10
Applications	Printer, multi-function printer etc.	Spin-dryer, grinder, Segway, transportation cart etc.	Fan, grinder, agriculture cart, spindle, pump etc.

1) Experimental data

current of the fabricated chip is 5 mA at 1.8 V (VDD), and 47 mA at 5 V (IOVDD+GVDD), and is 23 mA with a chip reset condition.

2. Target Motor Specifications

Rated powers of 32 W, 200 W, and 1,500 W for the PMSM are prepared to evaluate the fabricated sensorless chip.

Experiments include a speed control test and load adaptive tests. Table 1 shows the target PMSM specifications.

3. Sensorless Operations

Steady-state sensorless operation signals are generated by SMOs, and initial start-up behaviors are activated by forced induced signals from standstill. The average start-up time for a 1,500 W PMSM is around 500 ms; however, conditions relating to the start-up time were revised in the case of our target motors. In Fig. 7, sensorless signals, including the estimated BEMF alpha, $\hat{i}_\alpha$, and estimated BEMF beta, $\hat{i}_\beta$, are shown in the case of a 1,500 W PMSM operating at 1,000 rpm.

Figure 7(a) shows a stable sensorless operation, where the alpha and beta BEMF signals are well estimated with an angle of difference of ninety degrees. The same amplitude and period of the two signals are also shown.

Figure 7(b) shows the results of the sensorless angle (electrical degree) estimated using upper-estimated BEMF signals. The angle has a signal period of 33.3 Hz (= 0.03 s), which means that the mechanical speed of the target motor is 1,000 rpm (= 120/4 poles × 33.3 Hz) with a number of poles.

In this figure, to determine the accuracy of the estimated angle, an angle with a linear approximation is compared with the compensated motor position $\hat{\theta}$. The maximum error of the two angles is 8.8°, and the standard deviation is 7.06°. Figure 7(c) can be described through a histogram method of the angle differences. A total of 301 sample points are used. There are 115 samples within a 1° difference (38%), and 282 samples within a 5° difference (94%). The proposed sensorless algorithm works properly.

4. Speed Control Tests

The manufactured chip is made for speed control of the target motor operation. The reference speed of this chip can be controlled using a 100 rpm unit with an I2C control block. This chip enables sensorless operation from 300 rpm. Figure 8 shows the ability of the speed estimation and control using a 1,500 W PMSM. In this experiment, the reference speeds vary from 300 rpm to 3,000 rpm.

In Fig. 8(a), motor input currents are shown with U, V, and W phases in which the peak-to-peak of the phase current is 18 A and the root mean square (RMS) values of the phase current can be confirmed to be from 5.1 A to 5.6 A. Figure 8(b) describes three phase currents at 3,000 rpm. This work is also tested using a 1.5 kW PMSM, and a peak-to-peak U phase current is 125 A. The RMS values of the three phases are from 41.4 A to 45.4 A. In these experiments, it can be considered that a phase current does not have the same form and value as the
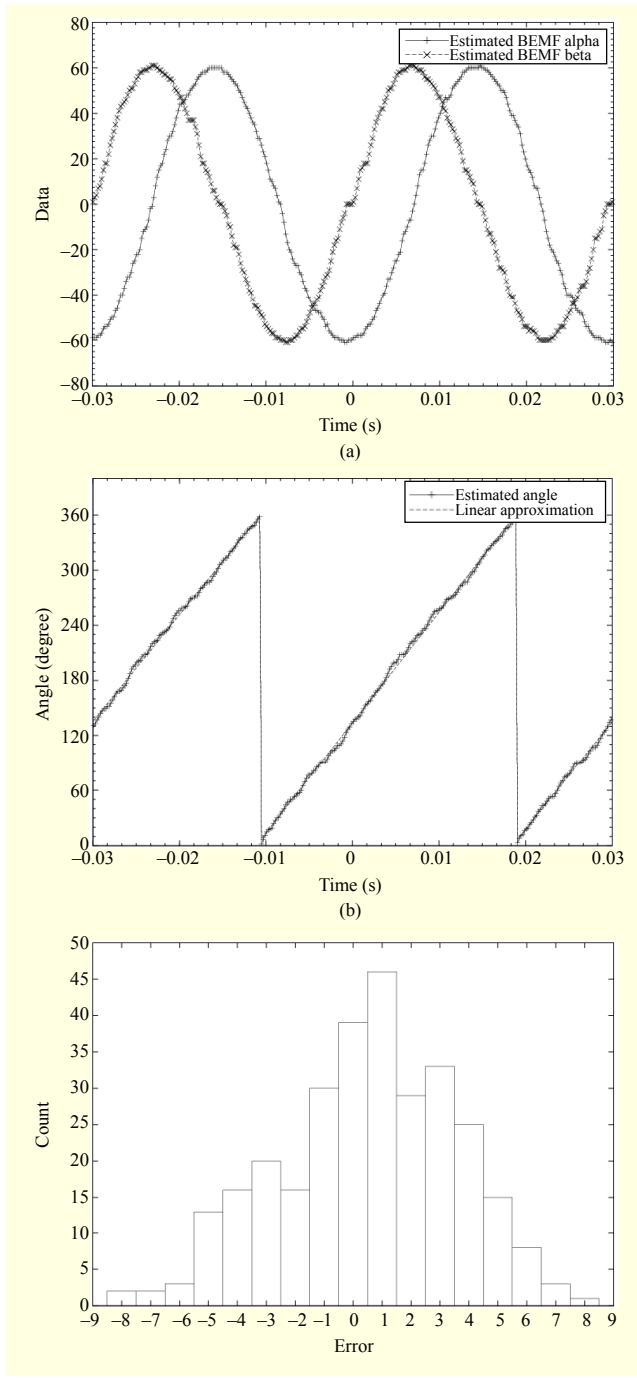
Fig. 7. (a) Estimated BEMF, (b) sensor-less angle, and (c) angle error distribution diagram for 1,500 W PMSM at 1,000 rpm.

others during motor operation.

5. Load-Adaptive Speed Control Tests

Load-adaptive tests are divided into three types — a fixed load, which is suitable in the case of many fan applications, such as those that are used in a refrigerator to maintain the
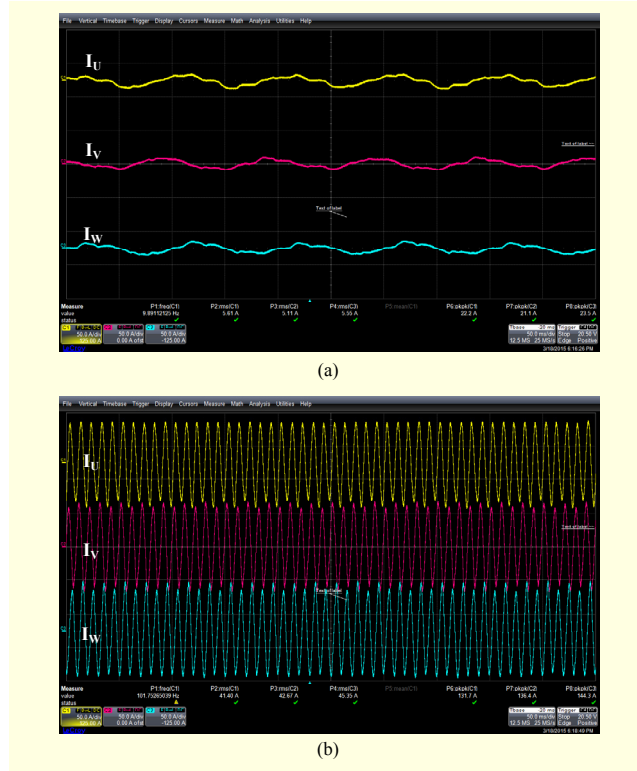

Fig. 8. Speed control tests: (a) 300 rpm and (b) 3,000 rpm.

icebox temperature; a pulse load test, in which steep load variations can be detected, such as in an automobile and the tub in a washing machine; and a continuous load test, which is capable of confirming the maximum point of efficiency.

A. Speed Control Tests with Fixed Load Variation

In the speed control tests of Section IV-4, load was not considered when calculating motor power. Motor power can be considered properly once load conditions are included. Figure 9 shows a fixed load test in which the load is 4.5 N·m, which is near the maximum rated load for a 1,500 W PMSM. Figure 9(a) shows a test at 300 rpm, and Fig. 9(b) shows a test at 3,000 rpm.

To calculate the system efficiency, the input current I_{PVDD} is also considered using the average input current value. Under a fixed load, when the reference speed is higher, the input current of the system at a high speed is higher than one at a low speed. This means that the input voltage is fixed at 48 V in a 1,500 W PMSM, and an increasing input power is related to an increasing input current for a proper operation. The fluctuation of the input current in Fig. 9(b) implies that the input current is affected by the motor rotation, and the power flow of the system is considered with gate driver input signals. The phase current is also detected at higher speed and load conditions. In Figs. 8(a) and 9(a), we can observe that the two phase currents do not share the same value owing to the different load
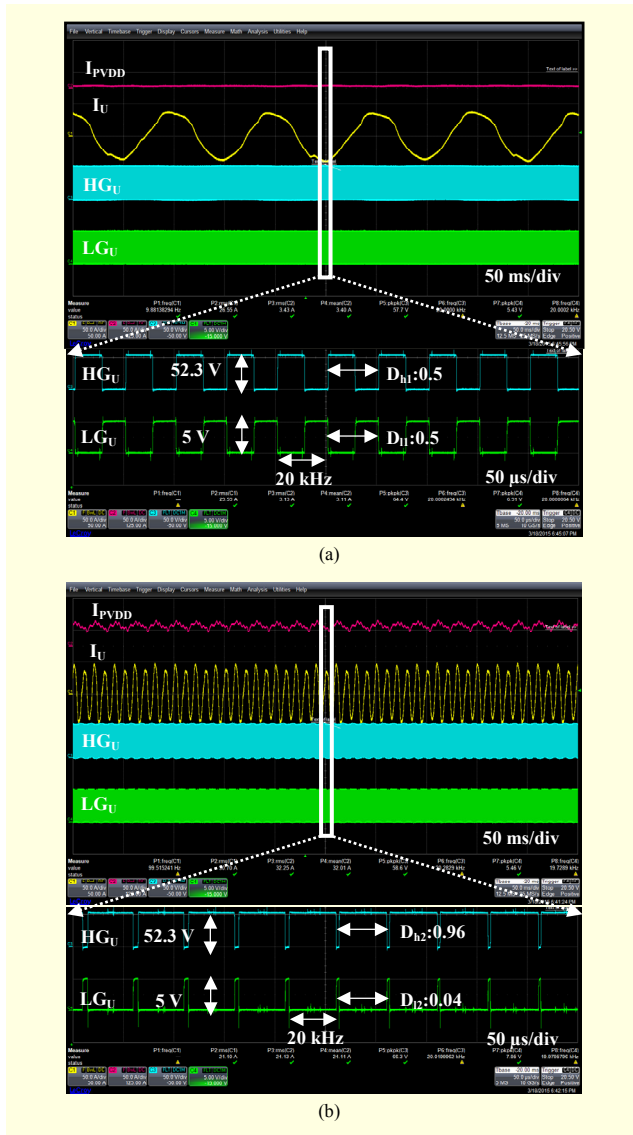
Fig. 9. Fixed loads (4.5 N·m) tests at (a) 300 rpm and (b) 3,000 rpm.

it works properly according to previous algorithms. The low-side gate driver signal LG_U is 5 V. While the speed increases, the duty variation of the gate driver signals is increased. At 300 rpm and 4.5 N·m, the duties of the gate driver signals, D_{h1} and D_{l1}, are 50% (Ton/T, where Ton indicates "on time," and T is the time period) and not varied. On the other hand, at 3,000 rpm and 4.5 N·m, the variation of the gate driver signals is high and the duties D_{h2} and D_{l2} are detected as 0.96 and 0.04, respectively. This implies that the duty variation increases with a high power output.

B. Speed Control Tests with Pulsed Load Variation

A washing machine has two operating modes — washing and drying [4]. In washing mode, a tub motor is needed to rotate at high torque and low speed. In drying mode, on the other hand, it rotates at low torque and high speed. For this application, tests on the load conditions are needed to implement a steep load variation and pulse load conditions.

Figure 10 shows the speed variations from 1,000 rpm to 3,000 rpm with a pulse load of 2 N·m. With pulse load variations, the input and phase currents are varied without an out-of-phase operation, maintaining the reference speed conditions. These results imply that the load variation is approximately 200 ms by controlling the on and off operation of the loads, and the speed control step in manufactured chips is 10 ms at 20 MHz; thus, the speed control and estimation functions are properly operated with pulse-load variations. While the reference speed varies by 1,000 rpm, 2,000 rpm, and 3,000 rpm without a load, the input currents are increased to 0.5 A, 6 A, and 10 A, and the peak-to-peak values of the phase current are operated at 25 A, 30 A, and 45 A. On the other hand, with pulse loads, the input currents are changed to 6 A, 16 A, and 30 A, and the peak-to-peak values of the phase currents are varied to 63 A, 100 A, and 145 A. These results imply that the manufactured chip is proper to operate the load variations.

C. Speed Control with Continuous Load Variations

Continuous load variation tests are utilized to verify and evaluate the target motor systems. A dynamo test is implemented for evaluating the motor systems in that it can detect the motor speed; input current and voltage; three phase currents and voltages; several system efficiencies; and the inverter and motor with continuous load variations. These test results are considered using a commercial motor module including the motor driver and inverter in Table 2, which can be compared to the ETRI motor module.

Table 2 shows the commercial and ETRI motor module specifications. The operating voltages and rated currents are different with the target motors. All commercial motor modules

conditions. A PMSM under a fixed load condition operating at the same speed as a PMSM without load will have the higher phase current. On the other hand, as another result, at 3,000 rpm, the phase and input currents (125 A and 41.4 A, respectively) in Fig. 8(b) are higher than those (100 A and 30.7 A, respectively) in Fig. 9(b). It may be possible that the power factor is higher according to an increasing load; thus, the phase and input current can be lower under a load condition. For the motor operations, high phase currents under light load conditions are not proper; thus, the operating conditions need to be changed to reduce the currents.

Gate driver signals HG_U and LG_U are shown with a speed variation under fixed load conditions. The frequency of both gate driver signals is designed to be 20 kHz. The voltage of high-side gate driver signal HG_U is 52.3 V (48 + 5 − 0.7); thus,

Fig. 10. Pulse load tests: (a) 1,000 rpm, (b) 2,000 rpm, and (c) 3,000 rpm.

Table 2. Commercial and ETRI motor module specifications.

Module	BL55A-M01 [16]	TMC-MD02 [17]	TMC-D07 [17]	This work
Motor power (W)	32	200	1,500	32–1,500
Operating voltage (V)	24	12–24	12–48	24–48
Rated current (A)	2	10	35 (Max. 50)	Max. 100
PWM method	Square wave	Square wave	Square wave	Sinusoidal wave
Position detection	Sensor (Hall)	Sensor (Hall)	Sensor (Hall)	Sensorless (SMO)
Speed control	External clock frequency change	Volume switch change	Volume switch change	I2C controlled by 100 rpm unit
Appearance				

Fig. 11. Speed controls of 32 W PMSM under continuous load variations.

are implemented using a square wave PWM method and hall-effect sensors that need external position sensors. This work employed various motor powers with one module, and sensorless operation is possible with a more efficient speed control compared to commercial modules.

Figure 11 shows the speed control abilities with continuous load variations and speed variations in a 32 W PMSM. In a commercial motor module, the reference speed input is controlled with an external clock frequency that cannot be easily regulated. This PMSM is up to 120 mN·m of the rated load; thus, the maximum experimental load is 100 mN·m with a step of 4 mN·m and a 2 s waiting time. The ETRI motor module is varied with a step of 2 mN·m and the same waiting
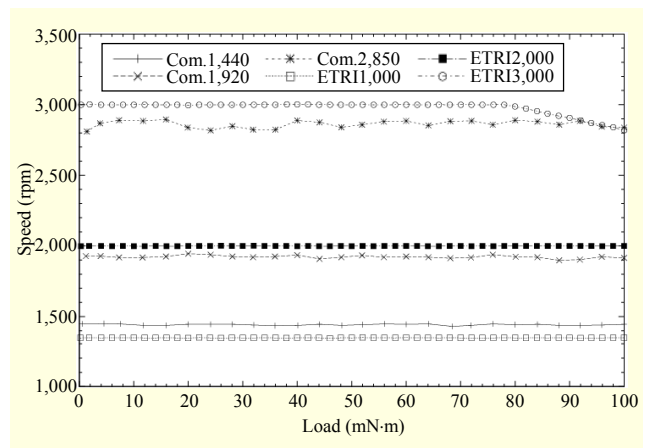
time for sensorless operation. At the 1,440 rpm reference speed of a commercial module, the speed is maintained near the reference level. The maximum speed is 1,450 rpm and the minimum speed is 1,430 rpm. The average speed is 1,442 rpm, and the error between the average and reference speeds is 2 rpm (reference − average). The speed deviation is 1.39% ((maximum − minimum) / average × 100).

In the ETRI module, at a 1,350 rpm reference speed, the experimental module with a fabricated chip is operated at a maximum speed of 1,351 rpm, minimum speed of 1,346 rpm, and average speed of 1,349 rpm, with a 1 rpm error and a 0.37% speed deviation. Between 1,000 rpm to 1,999 rpm, the speed control is 3.76-times higher than in a commercial module. The motor speed information for the 1,920 rpm and 2,850 rpm reference speeds in a 32 W motor is expressed in Table 3. As shown in Table 3, near a reference speed of 2,000 rpm, the speed deviation in our module is 16-times

higher, and near a reference speed of 3,000 rpm, the speed deviation is 17-times higher. Sensorless operation and the sinusoidal PWM method have several exertions to extract the parameters for proper BEMF signals. Our module can be implemented with sensorless parameter settings without an out-of-phase operation. The operation results for 200 W and 1,500 W motors are also shown in Table 3.

In a 200 W motor, the speed deviation in the commercial module is 0.50% at 1,000 rpm, 0.44% at 2,000 rpm, and 1.13% at 3,000 rpm; thus, the speed is decreased from 280 mN·m. On the other hand, the ETRI module is 5.64% at 1,000 rpm, 1.22% at 2,000 rpm, and 0.25% at 3,000 rpm when operating from 0 mN·m to 546 mN·m. The two modules are properly operated at reference speeds of 1,000 rpm and 2,000 rpm. However, our module at 1,000 rpm and 2,000 rpm has 20 rpm and 46 rpm higher errors from the reference speed, respectively. This means that the estimated BEMF signals are not properly detected and the sensorless gain and current gain needs to be suitably set. Occasionally, a higher speed error occurs when a parameter is not properly set. At 3,000 rpm, proper parameter settings occur, and the speed deviation is 0.25%, whereas for a commercial module, the deviation is 1.13%.

At 1,500 W, our module works suitably to operate the target motor at a full maximum load. With a speed volume switch in a commercial module, the speed errors are higher than those in our module. A speed deviation in our module can be realized with the same level as that of a commercial module.

Figure 12 shows the system efficiencies under various rated powers. The system efficiency is defined as the ratio of input power to motor output, which is a crucial factor in determining the performance of a motor module. The system efficiency

Table 3. Speed control characteristics.

M (W)	Module	Reference speed (rpm)	Maximum speed (rpm)	Minimum speed (rpm)	Average speed (rpm)	Speed error (rpm)	Speed deviation (%)
32	Com.	1,440	1,450	1,430	1,442	2	1.39
		1,920	1,945	1,898	1,922	2	2.45
		2,850	2,895	2,810	2,861	11	2.97
	ETRI	1,350	1,351	1,346	1,349	1	0.37
		2,000	2,001	1,998	1,999	1	0.15
		3,000[1]	3,001	2,996	2,999	1	0.17
200	Com.	1,000	1,001	996	999	1	0.50
		2,000	1,996	1,988	1,991	9	0.44
		3,000[2]	3,021	2,988	3,001	1	1.13
	ETRI	1,000	1,048	990	1,020	20	5.64
		2,000	2,055	2,030	2,046	46	1.22
		3,000[3]	3,002	2,995	2,999	1	0.25
1,500	Com.	1,000	1,060	1,050	1,055	55	0.95
		2,000	2,093	2,073	2,085	85	0.96
		3,000	2,868	2,855	2,863	137	0.44
	ETRI	1,000	1,011	988	999	2	2.30
		2,000	2,016	1,980	1,998	2	1.80
		3,000	3,009	2,995	2,999	1	0.47

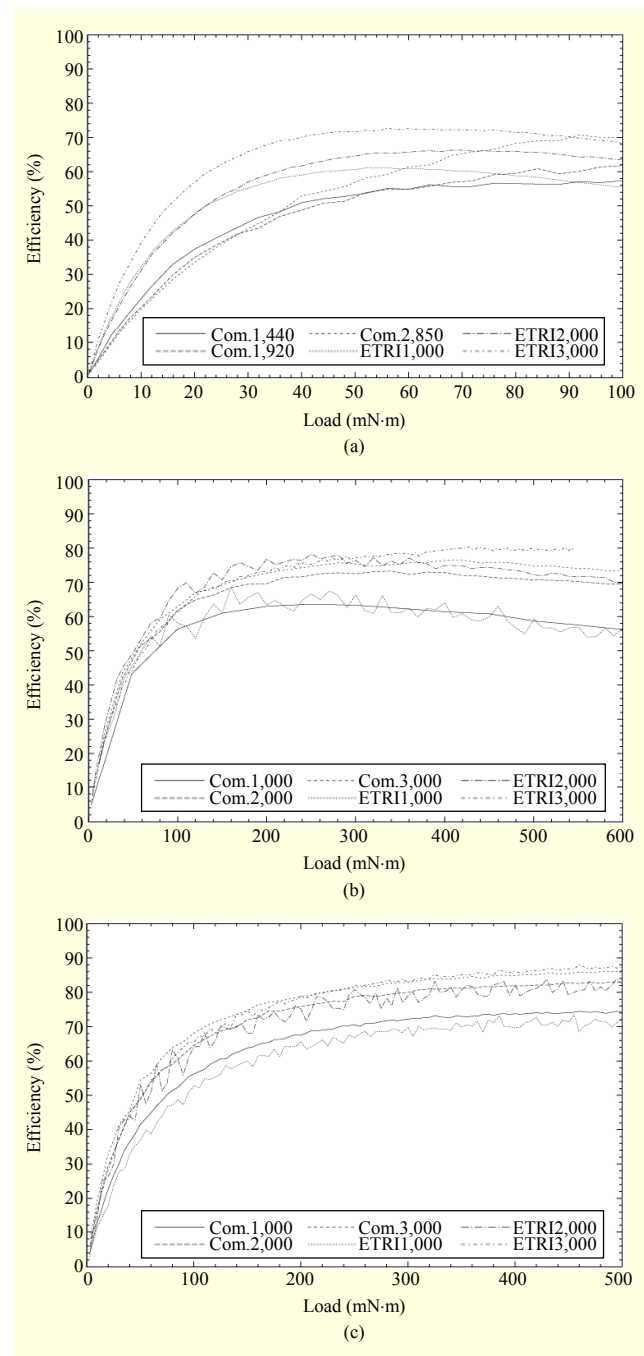Load up to 1) 80 mN·m, 2) 280 mN·m, and 3) 546 mN·m.

Fig. 12. System efficiencies of PMSM under continuous load variations for (a) 32 W, (b) 200 W, and (c) 1,500 W.

Table 4. System efficiency characteristics.

M (W)	Module	Reference speed (rpm)	Torque at maximum efficiency (mN·m)	Maximum efficiency (%)
32	Com.	1,440	100	57.4
		1,920	100	65.8
		2,850	100	47.9
	ETRI	1,350	56	61.2
		2,000	68	66.3
		3,000	56	66.3
200	Com.	1,000	250	63.6
		2,000	340	73.3
		3,000	420	76.5
	ETRI	1,000	160	68.6
		2,000	250	78.3
		3,000	427	80.3
1,500	Com.	1,000	5,000	74.5
		2,000	5,000	83.0
		3,000	5,000	86.2
	ETRI	1,000	5,000	73.5
		2,000	5,000	83.8
		3,000	5,000	88.1

depends on the resistance of the power MOSFET and the switching frequency; the proper settings were applied before the experiments. The maximum efficiency of the commercial module at 32 W is achieved at 100 mN·m, with 57.4% at 1,440 rpm, 65.8% at 1,920 rpm, and 47.9% at 2,850 rpm. The ETRI module, on the other hand, has different torque points at various speeds, with 56 mN·m at 1,350 rpm, 68 mN·m at 2,000 rpm, and 56 mN·m at 3,000 rpm. The maximum efficiencies of the ETRI module are higher than those of the commercial module. At near 100 mN·m, the efficiencies are similar with those of the commercial module. In a wide range of loads, the ETRI module has a higher efficiency than the commercial module, which means that when the output power is the same, the input power is lower. Table 4 shows the system efficiencies of other motors and modules. The results indicate that the ETRI module enables proper sensorless operations with a high system efficiency.

V. Conclusion

A PMSM driver IC chip including sensorless control functions was fabricated using gate drivers employing phase-current sensing technology. A motor module, including a manufactured chip, and inverters were implemented to evaluate several rated powers of a PMSM at 32 W, 200 W, and 1,500 W. The performances of a commercial module were compared with those of an ETRI module in terms of speed control and system efficiency. The speed control capabilities of the ETRI module are better than those of the commercial module. The system efficiency of our module is also better than the commercial module under different torque points. A fabricated chip without position sensors was shown to operate well and can reduce the system components and costs.

References

[1] Toshiba Semiconductor, *TB6588 Datasheet*, Toshiba Semiconductor, 2011. Accessed Feb. 24, 2013. http://toshiba.semicon-storage.com/info/docget.jsp?did=11516&prodName=TB6588FG

[2] Freescale Semiconductor, *Sensorless PMSM Vector Control with a Sliding Mode Observer for Compressors Using MC56F8013*, Freescale Semiconductor, 2008. Accessed Feb. 24, 2013. http://cache.freescale.com/files/microcontrollers/doc/ref_manual/DRM099.pdf

[3] S.M. Kazraji, R.B. Soflayi, and M.B. B. Sharifian, "Sliding-Mode Observer for Speed and Position Sensorless Control of Linear-PMSM," *Electr., Contr. Commun. Eng.*, vol. 5, no. 1, May 2014, pp. 20–26.

[4] S. Chi, Z. Zhang, and L. Xu, "Sliding-Mode Sensorless Control of Direct-Drive PM Synchronous Motors for Washing Machine Applications," *IEEE Trans. Ind. Appl.*, vol. 45, no. 2, Mar.–Apr. 2009, pp. 582–590.

[5] S.G. Kim et al., "Fabrication of Superjunction Trench Gate Power MOSFETs Using BSG-Doped Deep Trench of p-Pillar," *ETRI J.*, vol. 35, no. 4, Aug. 2013, pp. 632–637.

[6] F. Parasiliti, R. Petrella, and M. Tursini, "Sensorless Speed Control of a PM Synchronous Motor by Sliding Mode Observer," *Proc. IEEE Int. Symp. Ind. Electron.*, Guimaraes, Portugal, July 7–11, 1997, pp. 1106–1111.

[7] H. Lin, K.-Y. Hwang, and B.-I. Kwon, "An Improved Flux Observer for Sensorless Permanent Magnet Synchronous Motor Drives with Parameter Identification," *J. Electr. Eng. Technol.*, vol. 8, no. 3, 2013, pp. 516–523.

[8] Z. Ma and R. Kennel, "System-on-Chip Sensorless Control of PMSM Combining Signal Injection and Flux Observer," *Int. Power Electron. Motion Contr. Conf.*, Harbin, China, June 2–5, 2012, pp. 1201–1205.

[9] Y. Chang and Y. Tzou, "Single-Chip FPGA Implementation of a Sensorless Speed Control IC for Permanent Magnet Synchronous Motors," *Power Electron. Specialists Conf.*, Orlando, FL, USA, June 17–21, 2007, pp. 593–598.

[10] Z. Ma et al., "Model Based Design for System-on-Chip Sensorless Control of Synchronous Machine," *Sensorless Contr.*

Electr. Drives, Birmingham, UK, Sept. 1–2, 2011, pp. 85–89.

[11] A. Sathyan et al., "An FPGA-Based Novel Digital PWM Control Scheme for BLDC Motor Drives," *IEEE Trans. Ind. Electron.*, vol. 56, no. 8, Aug. 2009, pp. 3040–3049.

[12] Z. Qiao et al., "New Sliding-Mode Observer for Position Sensorless Control of Permanent-Magnet Synchronous Motor," *IEEE Trans. Ind. Electron.*, vol. 60, no. 2, Feb. 2013, pp. 710–719.

[13] S. Bejerke, *Digital Signal Processing Solutions for Motor Control Using the TMS320F240 DSP-Controller*, Texas Instruments, 1996. Accessed Feb. 24, 2013. http://www.ti.com/lit/an/spra345/spra345.pdf

[14] Y. Inoue et al., "Effectiveness of Voltage Error Compensation and Parameter Identification for Model-Based Sensorless Control of IPMSM," *IEEE Trans. Ind. Appl.*, vol. 45, no. 1, Jan.–Feb. 2009, pp. 213–221.

[15] C. Lee and P. Mok, "A Monolithic Current-Mode CMOS dc–dc Converter with on-Chip Current-Sensing Technique," *IEEE J. Solid-State Circuits*, vol. 39, no. 1, Jan. 2004, pp. 3–14.

[16] Moatech, "BL55 Series Motor BL55A-M01 Specification," Preprint. http://www.moatech.com/product/prod_bldc_02_u.asp

[17] TMtechi, "DC Driver (DC 12 V–48 V) Specification," Preprint. http://www.tmmotor.co.kr/?Page=p06c02.

Jimin Oh received his BS degree in electrical and electronic engineering and his MS degree in electrical engineering from Kyoto University, Japan, in 2008 and 2010, respectively. Upon graduating, he joined ETRI as a researcher. His research interests include motor driver IC design, power management IC design, nonlinear dynamics, and MEMS.

Minki Kim received his BS degree in electrical engineering and computer science from Kyungpook National University, Daegu, Rep. of Korea, in 2008 and his MS degree in electrical engineering and computer science from Seoul National University, Rep. of Korea, in 2010. Since 2010, he has been working at ETRI as a researcher. His research interests include wide band-gap power devices and power control systems.

Sewan Heo received his BS and MS degrees in electrical and electronic engineering from Korea Advanced Institute of Science and Technology, Daejeon, Rep. of Korea, in 2005 and 2007, respectively. He joined ETRI in 2007, where he is currently a senior researcher. His research interests include power converters, synchronous motor drives, digital/analog control circuits design, and renewable energy conversion in power systems.

Jung-Hee Suk received his BS, MS, and PhD degrees in electronics engineering from Kyungpook National University, Daegu, Rep. of Korea, in 2001, 2003, and 2007, respectively. His doctoral research involved the H.264/AVC codec algorithm. He joined ETRI in February 2007 as a researcher and now works for the NT Convergence Components Research Department. His current research interests include multi-media codecs; parallel processing of media data; efficient architectures of SoC; recognition algorithms for smart vehicles and mobile terminals; and motor control systems.

Yil Suk Yang received his BS, MS, and PhD degrees in electronics engineering from Kyungpook National University, Daegu, Rep. of Korea, in 1989, 1994, and 2008, respectively. Before joining ETRI in 1999, he was with LG Semiconductor, Seoul, Rep. of Korea. Since 1999, he has worked at ETRI's Basic Research Laboratory, where he has been engaged in research on low power circuit design, high energy efficiency circuit design, and power electronics design.

Ki-Tae Park received his BS degree and MS degrees at the Department of Electrical Engineering from Seoul National University, Rep. of Korea, in 1995 and 1997, respectively. Since 1997, he had worked for Samsung Electronics, Co., Ltd., Suwon, Rep. of Korea until he founded Iron Device Corporation, Seoul, Rep. of Korea in 2008, where he is CEO. His interests include mixed signal system LSI design, audio power amplifier IC, and power electronics.

Jinsung Kim received his BS degree at the Department of Electrical Engineering from Konkuk University, Seoul, Rep. of Korea, in 1998. From 1998 to 1999, he had worked for Samsung Electronics, Co., Ltd., Suwon, Rep. of Korea. From 2009 to 2008, he had worked for Fairchild Korea, Co., Ltd., Bucheon, Rep. of Korea. Since 2008 he has worked at Iron Device Corp., Seoul, Rep. of Korea as a circuit designer. His interests include mixed signal system LSI design, class D audio amplifier, and power electronics.